




Article

Microwave-Assisted Biodiesel Production Using UiO-66 MOF Derived Nanocatalyst: Process Optimization Using Response Surface Methodology

Shiva Prasad Gouda¹, Jasha Momo H. Anal^{2,3}, Puneet Kumar^{2,3}, Amarajothi Dhakshinamoorthy⁴ , Umer Rashid⁵  and Samuel Lalthazuala Rokhum^{1,*} 

¹ Department of Chemistry, National Institute of Technology Silchar, Silchar 788010, India

² Natural Products and Medicinal Chemistry Division, CSIR—Indian Institute of Integrative Medicine, Jammu 180001, India

³ Academy of Scientific and Innovative Research (AcSIR), Ghaziabad 201002, India

⁴ School of Chemistry, Madurai Kamaraj University, Madurai 625021, India

⁵ Institute of Nanoscience and Nanotechnology, Universiti Putra Malaysia, Serdang 43400, Malaysia

* Correspondence: rokhum@che.nits.ac.in

Abstract: The present work is on the transesterification of soybean oil to biodiesel under microwave irradiation using a biomass and MOF-derived CaO–ZrO₂ heterogeneous catalyst. The optimisation of different parameters was processed by adopting a central composite design for a response–surface methodology (RSM). The experimental data were fitted to a quadratic equation employing multiple regressions and investigated by analysis of variance (ANOVA). The catalyst was exhaustively characterised by XRD, TGA, FTIR BET, SEM, TEM, CO₂ TPD and XPS. In addition, the synthesized biodiesel was characterized by ¹H and ¹³C NMR, GCMS. The physicochemical properties of the biodiesel were also reported and compared with the ASTM standards. The maximum yield that was obtained after optimization using RSM was 97.22 ± 0.4% with reaction time of 66.2 min, at reaction temperature of 73.2 °C, catalyst loading of 6.5 wt.%, and methanol–to–oil ratio of 9.7 wt.%.

Keywords: biomass; biodiesel; heterogeneous catalyst; response surface methodology; transesterification



Citation: Gouda, S.P.; H. Anal, J.M.; Kumar, P.; Dhakshinamoorthy, A.; Rashid, U.; Rokhum, S.L. Microwave-Assisted Biodiesel Production Using UiO-66 MOF Derived Nanocatalyst: Process Optimization Using Response Surface Methodology. *Catalysts* **2022**, *12*, 1312. <https://doi.org/10.3390/catal12111312>

Academic Editors: Victorio Cadierno and Diego Luna

Received: 23 September 2022

Accepted: 21 October 2022

Published: 26 October 2022

Publisher's Note: MDPI stays neutral with regard to jurisdictional claims in published maps and institutional affiliations.



Copyright: © 2022 by the authors. Licensee MDPI, Basel, Switzerland. This article is an open access article distributed under the terms and conditions of the Creative Commons Attribution (CC BY) license (<https://creativecommons.org/licenses/by/4.0/>).

1. Introduction

Environmental concerns have risen because of the massive use of conventional resources, prompting calls for green and alternative resources [1]. Biodiesel production is vital all over the world, due to the pressures of decreasing fossil energy and a worsening environment. Biodiesels are long–chain fatty acids of methyl esters and are promising alternatives for conventional diesel engines, which can be synthesised by the transesterification of triglycerides with methanol [2,3]. For biodiesel production, traditional homogeneous catalysts are being phased out in favour of newly developed catalysts [4,5] Although homogeneous catalysts have been used, their low recyclability and strong corrosivity necessitate adequate disposal methods. Furthermore, homogeneous catalysts for biodiesel purification are expected to need a significant amount of water [6,7]. Heterogeneous catalysts, on the other hand, are profitable due to the relative ease with which they can be separated for reusability and to restrict mass exchange. Increasing the activity and efficiency of heterogeneous catalysts is crucial for green chemistry and sustainable biorefining [8–10]. In order to overcome the shortcomings of homogeneous catalysts, heterogeneous catalysts such as horn–shell–derived CaO [11], Ca–lipase@ZIF–67 [12], waste snail–shell–derived CaO [13], peanut–shell biochar [14], Fe₃O₄@SiO₂–SO₃H [1] and ZrSiW/UiO–66 [15], have been reported recently. Metals and their oxides (MMO) are often combined to develop new catalysts [16]. With each species functioning in synergy for greater catalytic performance, these mixed metal oxides can address issues that heterogeneous catalysts

confront. In addition to structural characteristics such as surface area, pore size, or stability, this may enhance the activity of the catalytic site or the magnetic separability [17]. Some of the mixed metal oxides that have been used recently for biodiesel production are Si–Ti MMO [18], CuO–CaO [19], Zn/MgAl(O) [20] and Co/Fe MMO [21]. CaO catalysts have a few drawbacks, such as leaching and deteriorations in stability [22]. To improve the stability and eliminate these catalysts' weaknesses, CaO can be immobilized on suitable carriers such as zeolites, alumina, silica, and MOFs [23]. The birch–templating pathway approach was designed to improve the pore structure of the catalyst and promote its reusability [24], as the pore structure would control the dispersity of the active site on the support [25]. ZrO₂ is a well-known amphoteric heterogeneous catalyst and catalytic support, possessing outstanding potential for performing simultaneous esterification–transesterification reactions of high-FFA feedstock to biodiesel [26]. Bellido et al. [27] reported the effect on nickel–catalyst activity of adding CaO to a ZrO₂ support in the dry reforming of methane, where ionic conductivity was claimed to be exploited by the extrinsic defects created by the replacement of Zr⁴⁺ cations in the lattice by Ca²⁺, with subsequent generation of oxygen vacancies to maintain electroneutrality. Xia et al. [28] prepared a CaO–ZrO₂ solid–base catalyst for biodiesel synthesis using a urea–nitrate combustion method for biodiesel synthesis with a conversion of 93.9%.

Metal–organic frameworks (MOFs) have demonstrated intrinsic characteristics such as a large specific surface area, a crystalline open structure, and tunable functions as an improved porous material for the fabrication of solid catalysts [29]. MOF–based solid catalysts are frequently created via post–synthesis modification of MOFs by loading different acid–base species [30]. UiO–66 MOF is one of the most explored MOFs and has been used in various fields of science in recent years. UiO–66 is made up of Zr₆O₄(OH)₄ nodes with six Zr⁴⁺ ions in octahedral geometry and four oxygen atoms or hydroxyls at the facet centres. Each Zr atom is coordinated with eight oxygen atoms in a square antiprismatic geometry by twelve terephthalate (BDC) ligands [31].

Creating a new approach to metal oxide synthesis/porous carbon nanocomposite techniques has received much attention over time as the materials possess high porosity and a modifiable shape and pore size without any additional carbon sources [32]. However, the use of waste materials as a catalyst source reduces the overall cost of biodiesel synthesis while also enabling for the recycling of natural mineral supplies, making the process green and environmentally beneficial. Thus, in the present work there is a reconciliation of ZrO₂–supported, biomass–derived CaO, a heterogeneous catalyst, to explore its MOF application. UiO–66 is used as a precursor and template to produce ZrO₂/C material as a support to snail–shell–derived CaO, which provides a synergistic effect, owing to the amphoteric nature of ZrO₂ and the basic trait of CaO, to produce biodiesel from soybean oil by means of a transesterification process. The maximum biodiesel yield from soybean oil was investigated by a statistical optimization process using response–surface methodology (RSM). The influence of process–input variables such as temperature, catalyst loading, methanol/oil ratio (MTOR) and reaction time, as well as their interactions, on biodiesel yield were evaluated using central composite design (CCD).

2. Results and Discussion

2.1. Catalyst Optimization

Effect of CaO Loading and Activation Temperature on Catalytic Activity

The optimum CaO loading, and activation temperature required for the catalyst preparation was investigated by adding CaO in a range of 30–70 wt.% and the activation temperature varied from 600–750 °C, respectively (shown in Figure 1). The conversion of soybean oil to biodiesel was found to be increased with the increase in CaO loading from 30–50 wt.%, while further increment to 60 and 70 wt.% caused a decrease in the conversion rate. Thus, the CaO loading of 50 wt.% under the optimised condition resulting in the conversion of 98.03% was chosen to be the equilibrium amount of CaO required for the preparation of the high–conversion–providing catalyst. Activation temperature, on other

hand, also has a vital role in the catalyst preparation, where the activation temperature also showed a similar kind of trend upon moving from 600 °C to 750 °C. The conversion at 600 °C was 82.5%, which increased to 98.03% upon increasing the temperature to 650 °C. Further, activating at 700 and 750 °C resulted in a decrease in conversion to 92.4 and 85.3%, respectively. Thus, 650 °C was chosen to be the equilibrium activation temperature for the effective working of the catalyst.

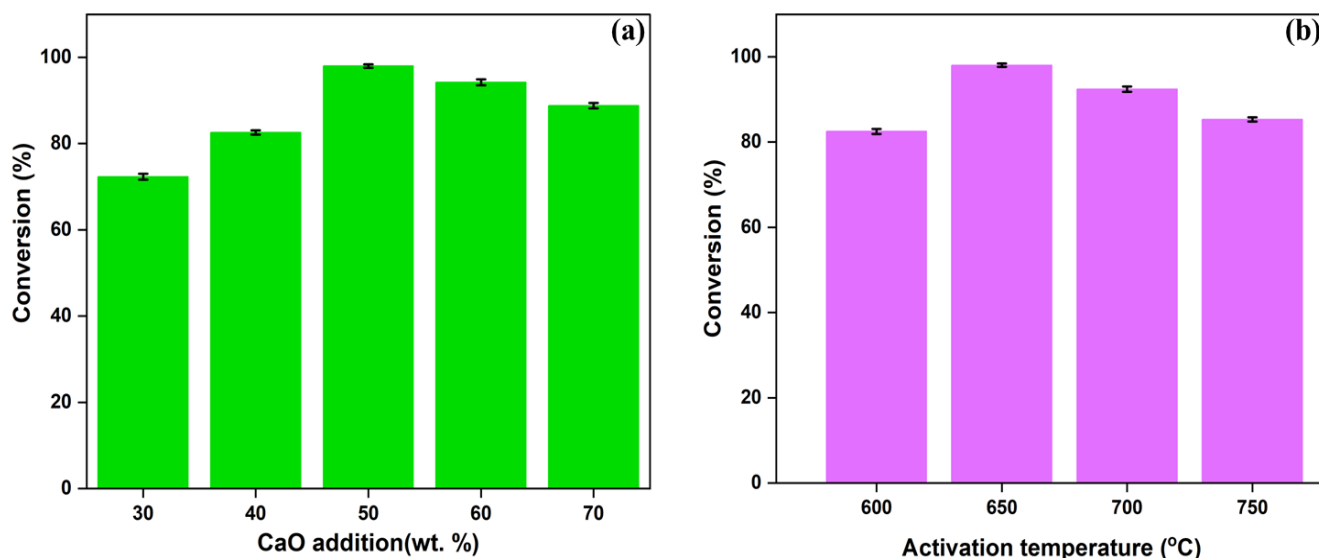


Figure 1. Effect of (a) CaO loading and (b) activation temperature on catalytic activity under optimised condition.

2.2. Catalyst Characterisation

2.2.1. XRD and TGA

The XRD of the CaO–ZrO₂ catalyst confirmed the successful incorporation of CaO into the lattice of ZrO₂ as the major peaks of snail–shell–derived CaO were absent (as shown in Figure 2a) in the XRD pattern of CaO–ZrO₂, which is in line with the reported literature [33]. The snail–shell–derived CaO used in this study was compared with pure CaO (Figure S2a) and coincides with all the XRD peaks of pure CaO, while a few peaks of Ca(OH)₂ also appeared due to uptake of moisture. In this study, UiO–66 was used as sacrificial template to form mixed phases of monoclinic zirconia (m–ZrO₂) and tetrahedral zirconia (t–ZrO₂). Jannah et al. [34] reported that UiO–66 calcination between 500–800 °C results in the formation of mixed phase zirconia. Thus, in Figure S2b, it can be clearly distinguished that the UiO–66 derived ZrO₂ consisted of both XRD peaks of m–ZrO₂ and t–ZrO₂. The XRD pattern of CaO–ZrO₂ nanocatalyst has diffraction peaks at 17.9°, 24.06°, 24.46°, 29.6°, 32.2°, 39.69°, 43.30°, 47.50°, 55.11° and 64.32° that correspond to m–ZrO₂ planes of (100), (011), (110), (11 $\bar{1}$), (111), (21 $\bar{1}$), (102), (21 $\bar{2}$), (221) and (032), respectively (JCPDS file No. 79–1769), while diffraction peaks at 31.4°, 36.09°, 50.5° and 63.18° corresponding to t–ZrO₂ planes of (101), (110), (200) and (202), respectively (JCPDS file No. 78–1807).

As depicted in Figure 2b, the mass loss of the nanocatalyst precursor was observed in three stages, where the first mass loss was in the range 380–420 °C due to the decomposition of Ca(OH)₂. The second stage of mass loss was observed in the range 490–540 °C and attributed to the degradation of UiO–66 (Zr) [35] and the third mass loss was observed due to the decomposition of CaCO₃ [13] that possibly could have resulted from the uptake of dissolved CO₂ by CaO in water during wet impregnation or while drying in the oven during the precursor–synthesis processes. However, further calcination of the precursor at 650 °C in the presence of an inert environment for 2 h during the catalyst synthesis would reconvert traces of CaCO₃ to CaO.

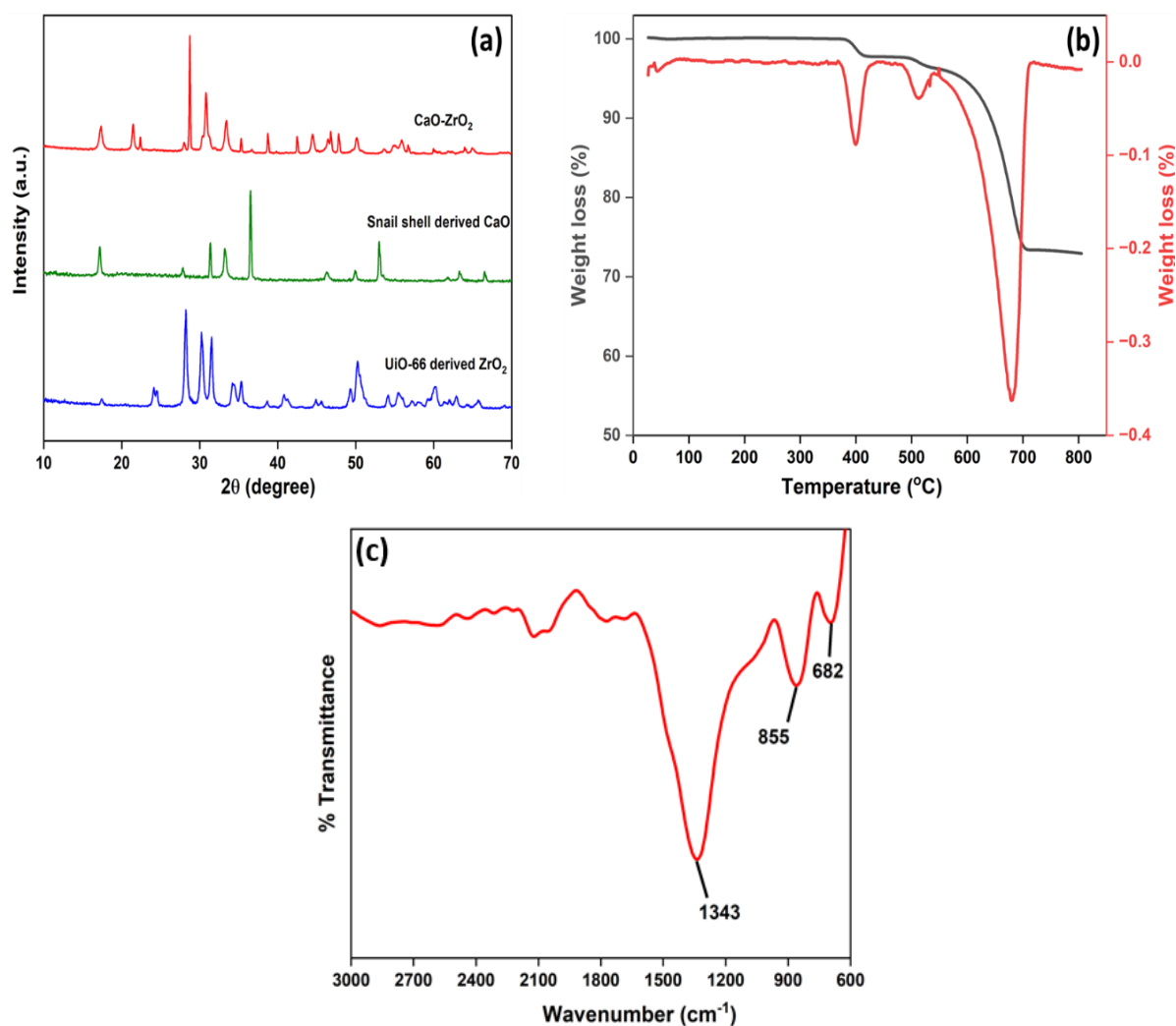


Figure 2. (a) XRD of the catalyst CaO–ZrO₂, (b) TGA of the catalyst precursor, and (c) FT–IR of the catalyst.

The FT–IR spectra of the catalyst in Figure 2c showed three major peaks of CaO–ZrO₂ where the 1200–1500 cm⁻¹ region peak could be ascribed to the overlapping of Ca–O and Zr–O stretching vibrations while the other two peaks at 682 and 855 cm⁻¹ profoundly confirmed the generation of Ca–O–Zr heterolinkages as Zr⁴⁺ ions partly substituted by Ca²⁺ ions and the transition of conventional m–ZrO₂ to t–ZrO₂, respectively. This was speculated by Zhang et al. [36] and is also quite in agreement with the XRD patterns of the catalyst.

2.2.2. BET

The catalyst's specific surface area and pore volume were determined by its N₂ adsorption/desorption isotherm, which indicated a type IV isotherm. (Figure 3) [35]. The surface area and pore volume of the catalyst CaO–ZrO₂ was found to be 7.9 m² g⁻¹ and 0.013 cc g⁻¹. The pore–size distribution analysis (inset, Figure 3) for the catalyst revealed a pore diameter of 2.2 nm.

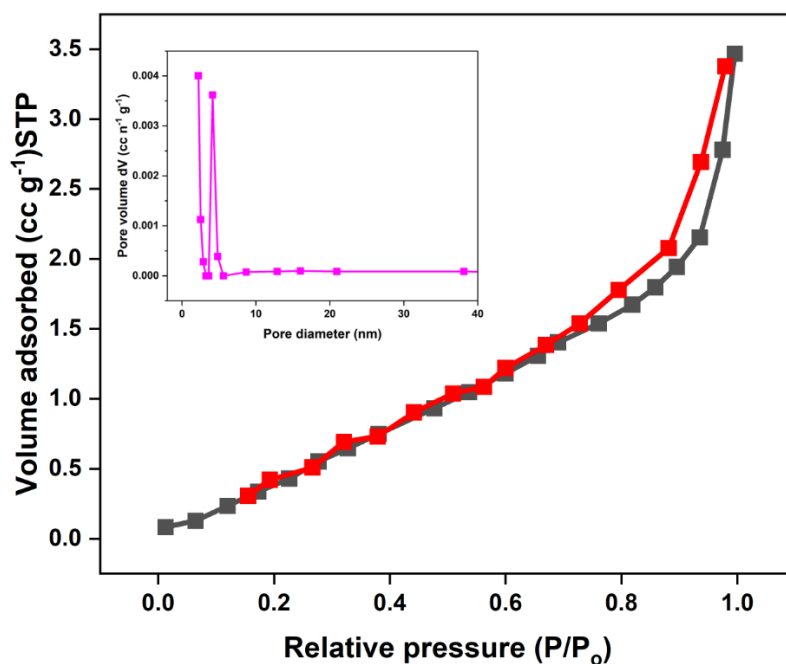


Figure 3. N_2 adsorption and desorption curve for the catalyst $CaO-ZrO_2$.

2.2.3. Basicity of Catalyst

The basic strength and the relative amount of surface basic sites on the $CaO-ZrO_2$ catalyst were studied by CO_2 -TPD. There were three desorption peaks, indicating the coexistence of three different types of adsorption sites with distinct basicity on the surface of the solid catalyst (Figure 4). The peaks at 415 °C and 520 °C could be ascribed to weak basic sites of ZrO_2 because of the coexistence of two zirconia phases ($t-ZrO_2$ and $m-ZrO_2$) [34,37]. This result was also corroborated by the XRD patterns, as shown in Figure S2b. The peak at 710 °C could be ascribed to the strong basic site upon introducing CaO loading to the ZrO_2 support [33,38]. The total basicity from the three basic sites was found to be 3.9 mmol g^{-1} .

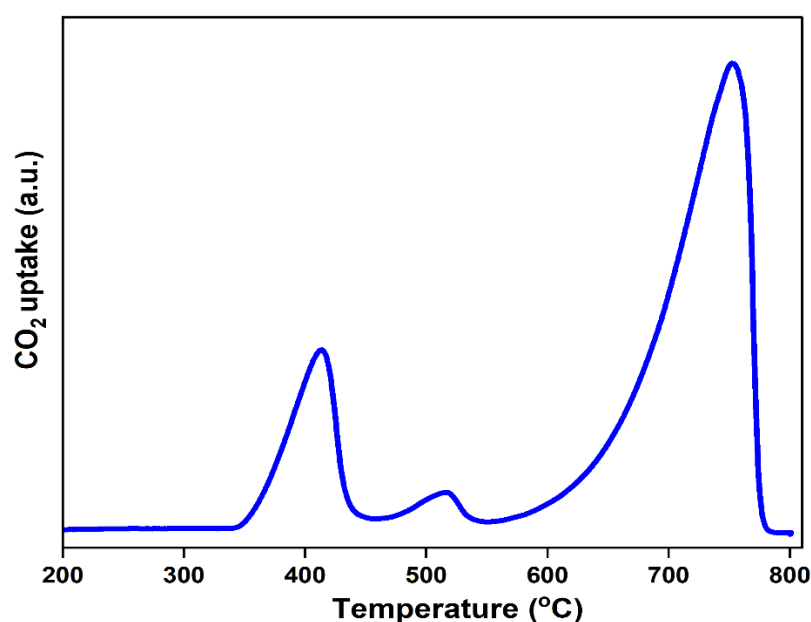


Figure 4. CO_2 -TPD profile of $CaO-ZrO_2$ catalyst.

2.2.4. SEM–EDS

SEM–EDS analysis (Figure 5a–c) was used to investigate the surface morphology of the CaO–ZrO₂ catalyst. After being loaded with calcium oxide and activated at 650 °C, homogeneous, although not perfect, size distribution of spherical particles was generated for CaO–ZrO₂ (Figure 5c). The EDX was also shown in Figure 5i, which highlighted the presence of Ca, O, Zr and C with relative atomic ratios and weight percentages of 29.14, 27.32, 7.16 and 36.38, respectively. The corresponding EDX elemental maps (Figure 5d–f) showed the distribution of calcium (yellow), oxygen (green), zirconium (pink) and carbon (red) in the CaO–ZrO₂ catalyst.

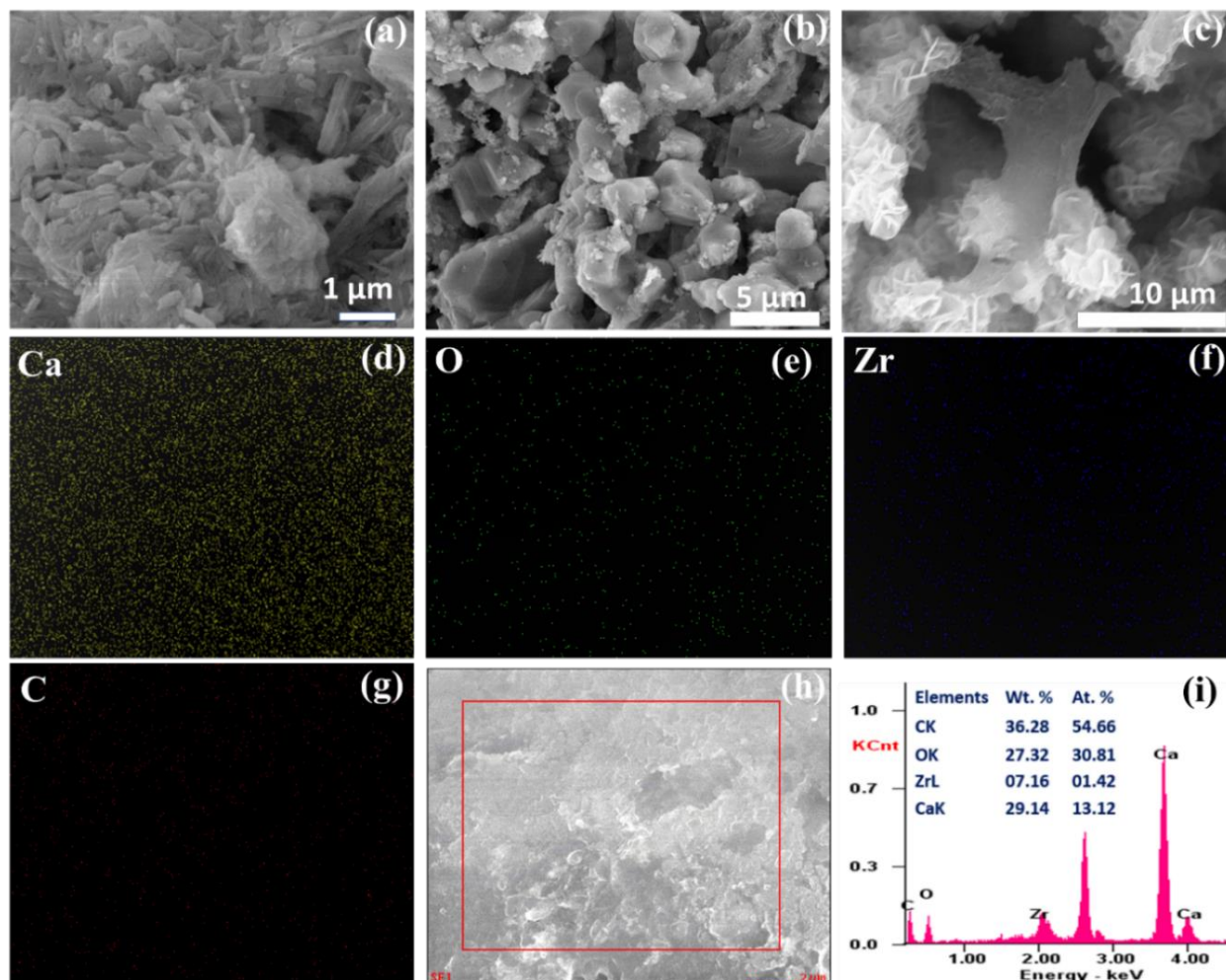


Figure 5. Representative SEM micrographs of CaO–ZrO₂ (a–c), elemental mapping of Ca (d), O (e), Zr (f), C (g) and EDS (h,i).

2.2.5. TEM

To study the structural features, TEM studies were performed and represented in Figure 6. The obtained TEM micrograph showed uniform distribution of nanoparticles with an average particle size of 33.98 nm (Figure 6c). It confirmed the spherical size of particles supporting the SEM micrograph results and displayed lattice fringes, shown in Figure 6a.

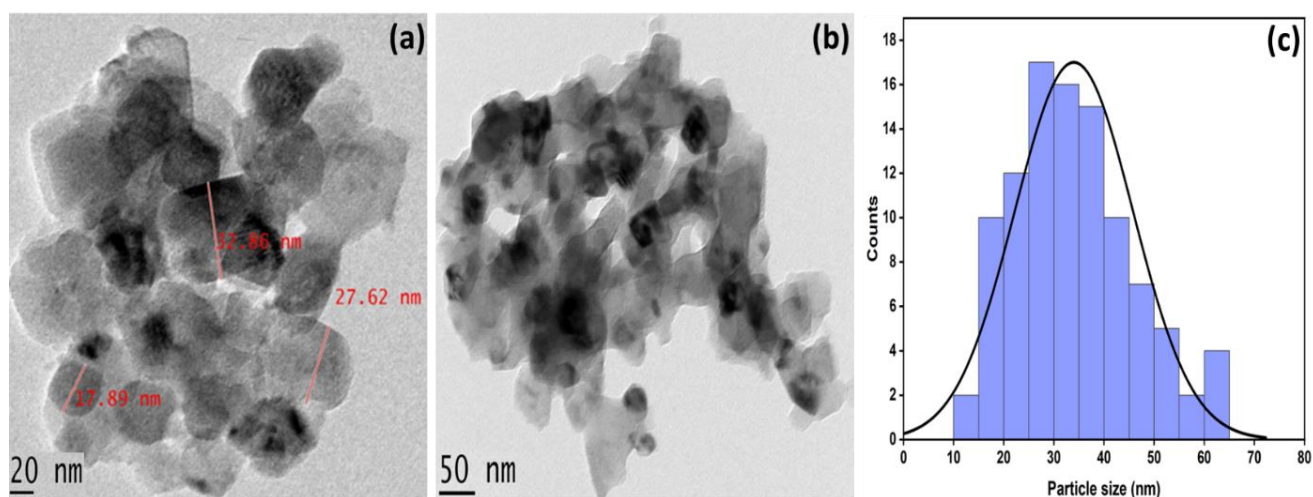


Figure 6. TEM graphs of (a) 20 nm, (b) 50 and (c) particle size distribution curve of the CaO–ZrO₂ catalyst.

2.2.6. XPS

The wide XPS spectrum showed the peaks of Ca2p, Zr3d, C1s and O1s in carbon-supported CaO–ZrO₂ catalyst (Figure S1). The Ca spectrum of CaO–ZrO₂ catalyst exhibited two peaks at 347.38 and 350.88 eV (Figure 7a) corresponding to Ca2p_{3/2} and Ca2p_{1/2}, respectively. The binding–energy separation due to spin–orbit splitting of Ca2p is 3.5 eV, which is in agreement with the CaO–MIL–100 (Fe) catalyst reported by Li et al. [39]. The two characteristic signals of Zr3d (Figure 7b) at 181.68 and 183.98 eV are ascribed to Zr–O bonds representing 3d_{5/2} and 3d_{3/2}, respectively [40,41]. The presence of carbon (C1s, Figure 7c) as support from the catalyst exhibits a strong peak at 285.8 eV and a weak peak at 287.28 eV, attributed to the presence of carbonate [39]. The O1s exhibit a single broad overlapped peak (due to CaO and ZrO₂) representing the metal–oxide lattice oxygen species [35,42].

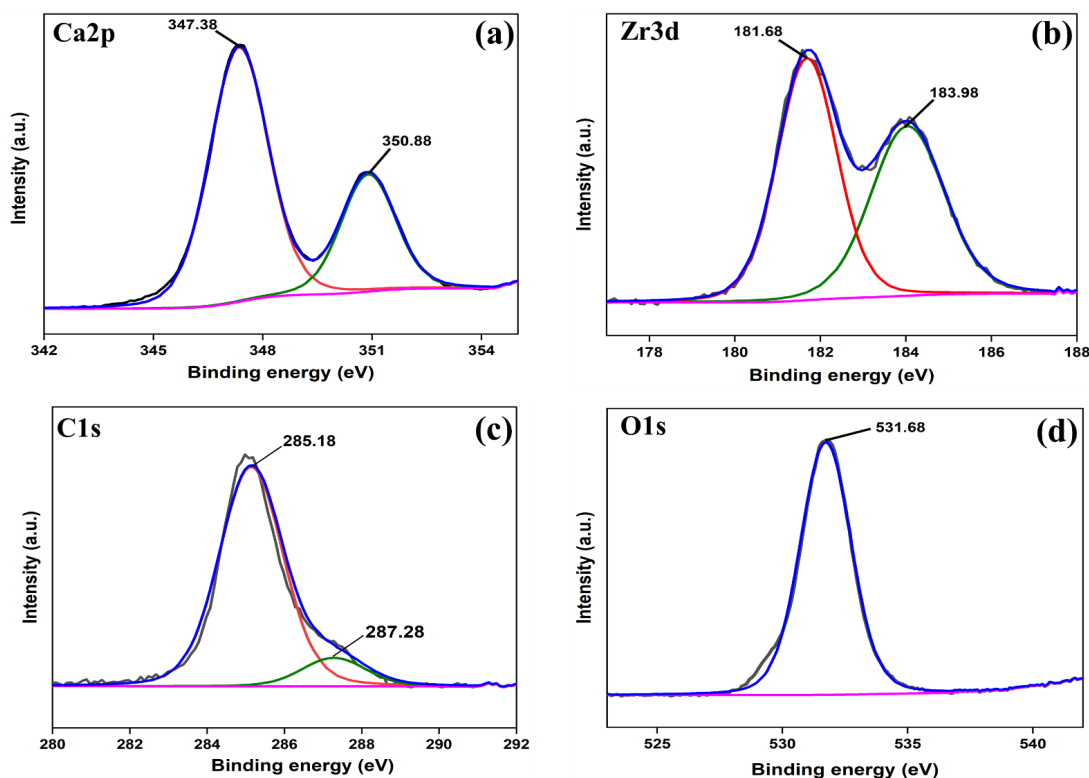


Figure 7. Representative deconvoluted XPS pattern of (a) Ca2p, (b) Zr3d, (c) C1s and (d) O1s.

2.3. Transesterification of Soybean Oil

The formation of biodiesel from soybean oil was estimated by employing the CaO–ZrO₂ catalyst. The ¹H and ¹³C NMR spectra of the synthesized biodiesel are shown in Figure S3. The conversion of soybean oil to biodiesel was determined by the ratio of the integrated areas of the peaks at 3.61 ppm (methoxy protons) and 2.31 ppm (α-CH₂ protons). The multiplets at 5.3 and 4.08 ppm indicate the presence of olefinic and glyceridic protons, respectively. Additionally, the presence of the sharp peak at 3.61 ppm for the methyl protons of ester confirms the formation of fatty acid methyl esters (FAMES). The following mentioned formula was used for evaluating soybean–oil conversion to biodiesel.

$$\text{Conversion (C)\%} = 100 \times \left(\frac{2A_{\text{Me}}}{3A_{\text{CH}_2}} \right) \quad (1)$$

where A_{Me} is the integral area portion of –OCH₃ and A_{CH₂} the area of –CH₂. The biodiesel yield was calculated by Equation (2) [43].

$$\text{Yield (\%)} = \frac{\text{Weight of biodiesel produced}}{\text{Weight of soybean oil used}} \times 100 \quad (2)$$

The FT–IR peaks of biodiesel shown in Figure S4 were similar to the reported literatures of Laskar et al. [13,43] and Kaewdaeng et al. [44]. The major peak region from 1800–1700 cm^{−1} ascribed to C=O stretching while 1452 and 1182 cm^{−1} peaks corresponded to asymmetric stretching of –CH₃ and O–CH₃ stretching, respectively.

GC–MS of Synthesized Biodiesel

The synthesized soybean–oil biodiesel composition was determined by GC–MS studies and gas chromatography as shown in Figure 8. The soybean–oil biodiesel composition studied using GC–MS with respect to the retention time, is summarized in Table 1. The major constituents were 9,12–octadecadienoic acid (Z, Z), methyl ester (47.19%), 9–octadecenoic acid, methyl ester (34.41%) and methyl stearate (5.51%).

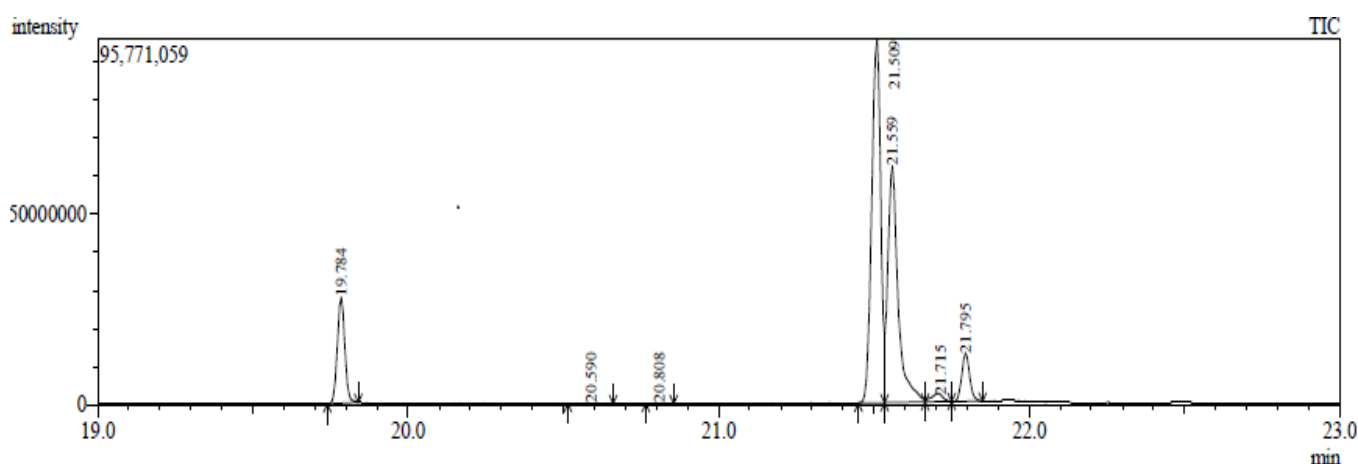


Figure 8. GC–MS of synthesised biodiesel.

Table 1. Chemical composition of soybean biodiesel.

Peak No.	Retention Time (min)	Identified Compounds	Composition (%)	Corresponding Acids
1	19.784	Hexadecanoic acid, methyl ester	11.23	C16:0
2	20.590	11,14–Eicosadienoic acid, methyl ester	0.20	C20:2
3	20.808	Heptadecanoic acid, methyl ester	0.10	C17:0
4	21.509	9,12–Octadecadienoic acid (Z, Z), methyl ester	47.19	C18:2
5	21.599	9–Octadecenoic acid, methyl ester	34.41	C18:1
6	21.715	9,12,15–Octadecatrienoic acid, methyl ester	1.37	C18:3
7	21.795	Methyl stearate	5.51	C18:0

2.4. Modelling Results and Data Analysis

The significance of the model structure and individual parameters impacting the response was determined by the Fischer test (F-value) in an ANOVA analysis. The relationship between biodiesel yield and independent factors was established using regression analysis and a coded second–order polynomial equation, as shown in Equation (1). The results of the transesterification reactions investigated with soybean oil under a microwave–aided system are presented in Table 2.

Table 2. Design of experiments for modelling biodiesel yield based on RSM–CCD method.

Std	Run	Time (min) (A)	Temperature (°C) (B)	Catalyst Loading (wt.% I)	MeOH: Oil (Molar Ratio) (D)	Actual Value Yield (%)	Predicted Value Yield (%)
21	1	60	70	2	10	75.83	76.36
18	2	90	70	6	10	86.35	85.55
14	3	75	60	8	12	81.23	81.7
16	4	75	80	8	12	88.67	88.85
17	5	30	70	6	10	75.42	76.3
27	6	60	70	6	10	95.8	96.43
4	7	75	80	4	8	80.16	79.78
29	8	60	70	6	10	96.42	96.43
12	9	75	80	4	12	85.24	85.64
26	10	60	70	6	10	96.63	96.43
19	11	60	50	6	10	87.64	87.49
22	12	60	70	10	10	82.38	81.93
6	13	75	60	8	8	83.66	83.9
15	14	45	80	8	12	76.01	75.7
11	15	45	80	4	12	78.01	77.42
28	16	60	70	6	10	96.51	96.43
10	17	75	60	4	12	79.02	78.68
7	18	45	80	8	8	80.56	80.55
24	19	60	70	6	14	70.6	70.69
13	20	45	60	8	12	74.21	74.24
8	21	75	80	8	8	86.88	87.25
2	22	75	60	4	8	76.03	76.61
20	23	60	90	6	10	91.89	92.12
30	24	60	70	6	10	96.6	96.43
5	25	45	60	8	8	83.01	82.88
3	26	45	80	4	8	78.21	78.01
25	27	60	70	6	10	96.63	96.43
23	28	60	70	6	6	73.47	73.47
1	29	45	60	4	8	81.04	80.51
9	30	45	60	4	12	76.23	76.13

The actual biodiesel yields obtained from the experiments conducted in the laboratory ranged from 70.60 to 96.63 wt.%. The model equation relating to the biodiesel yield as the response to the independent variables in term of the coded factors is described as

$$\text{Biodiesel yield} = 98.71 + 2.31 A + 1.16 B + 1.39 C - 0.6946 D + 1.42 AB + 1.23 AC + 1.61 AD + 0.044 BC + 0.9481 BD - 1.07 CD - 4.44 A_2 - 2.22 B_2 - 4.89 C_2 - 6.66 \quad (3)$$

where A is the reaction time, B is the reaction temperature, C is the catalyst loading (wt.%) and D is the MTOR (molar ratio).

The experimental results of ANOVA were performed and tabulated in Table 3. They comprises tests such as Fischer's statistical test (F-value); the *p*-value defines the probability of having an F-value of any size, and the sum of squares determines the relevance of parameters towards the model performance [45]. Any process parameter or model with a higher F-value has greater significance in the process. The F-value for the chosen quadratic model was 448.88, which is large enough to demonstrate the model's importance. It was also shown that noise had merely a 0.01% chance of causing such a large F-value. As a result, the model could be useful for optimizing biodiesel yield from soybean oil utilizing a CaO–ZrO₂ supported heterogeneous catalyst. A *p*-value < 0.05 indicates that the model's relevant term is significant. The linear terms (time, temperature, catalyst loading, and MTOR) are all significant, as shown in Table 3. All interactions and quadratic terms were found to be significant, except for the temperature–catalyst loading interaction. The statistical analysis of the entire process was performed and summarized in Table 4. The perfect fit of the experimental data in the chosen model can be explained by the obtained correlation coefficient R² of the model, 0.9976. An adequate precession was determined for the model, 66.42—above 4 is desirable [46]—as it measures the signal–to–noise ratio and this confirms that the model can be used to navigate the design space. The % CV was 0.655 for the model where a value < 10% is desirable, indicating a reasonable correlation between actual and predicted yield values.

Table 3. Design matrix, actual and predicted biodiesel yields for the transesterification.

Source	Sum of Squares	df	Mean Square	F-Value	<i>p</i> -Value	
Model	1888.16	4	134.87	448.88	<0.0001	significant
A–Time	128.21	1	128.21	426.7	<0.0001	
B–Temp	32.22	1	32.22	107.25	<0.0001	
C–CL	46.45	1	46.45	154.61	<0.0001	
D–MTOR	11.58	1	11.58	38.54	<0.0001	
AB	32.23	1	32.23	107.28	<0.0001	
AC	24.23	1	24.23	80.65	<0.0001	
AD	41.57	1	41.57	138.36	<0.0001	
BC	0.0315	1	0.0315	0.1049	0.7505	
BD	14.38	1	14.38	47.87	<0.0001	
CD	18.17	1	18.17	60.47	<0.0001	
A ²	412.1	1	412.1	1371.57	<0.0001	
B ²	75.23	1	75.23	250.39	<0.0001	
C ²	512.15	1	512.15	1704.58	<0.0001	
D ²	1016.82	1	1016.82	3384.23	<0.0001	
Residual	4.51	15	0.3005			
Lack of Fit	3.99	10	0.3995	3.9	0.0731	not significant
Pure Error	0.5123	5	0.1025			
Cor Total	1892.67	29				

Table 4. Statistical parameters estimated from the ANOVA study for the model.

Std. Dev.	0.5481	R ²	0.9976
Mean	83.68	Adjusted R ²	0.9954
C.V.%	0.6551	Predicted R ²	0.9875
		Adeq Precision	66.4194

In Figure 9a, the normal distribution probability was plotted against studentized residuals. The data points were distributed in a linear pattern, indicating that the studentized

residuals have a normal distribution that supports the regression results, as opposed to an abnormal S–shape curve, which is considered to be faulty for the model and may arise due to confidence–interval and p -value inaccuracy. The studentized residuals were plotted against predicted yield in Figure 9b. The residuals were distributed randomly on the plot within the limit of ± 3 , indicating that the model was adequate and implying that the predicted values of the observation were unrelated to the response values [6]. The residual vs. run plot for all experimental runs in the biodiesel production is shown in Figure 10a. From the plot, an experimental run with a large residual can easily be spotted. Independent residuals revealed no patterns or trends. The patterns in the points could imply that residuals close together are connected and thus not independent. On the plot, the residuals should ideally fall randomly around the central line. In Figure 10a, the points were distributed randomly around the line within the limits, indicating the accuracy and correctness of the model without any data error. The actual value and predicted value (in Figure 10b) for all responses were close to each other. Therefore, this observation shows that the model is suitable for the empirical data and could be used in the prediction of maximum biodiesel yield.

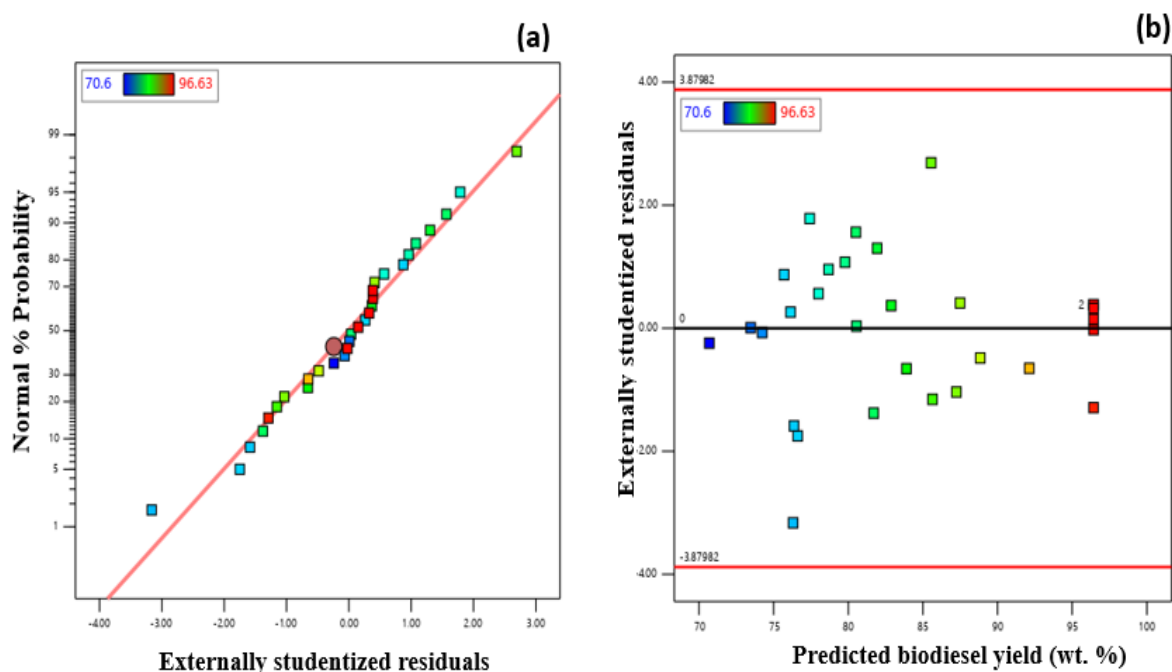


Figure 9. Diagnostic plots (a) Normal plot of residuals and (b) studentized residuals vs. the predicted biodiesel yield.

The perturbation plot in Figure 11 describes the most sensitive factor and its effect on biodiesel yield, keeping other factors constant to their centre values. The response was drawn by altering one element at a time over its defined range while retaining the other factors at their middle levels as constant values. The major effect of a variable over the yield is determined by the steepness of its slope. Thus, from the perturbation plot, we can clearly observe that from the lower level (-1) to the middle level (0), the dominant factor is A, as it has the steepest slope, followed by C, D and B, respectively. On the contrary, the process variable D has a dominant effect from the middle level (0) to the higher level (1). That with the increase in time from 45 to 60 min there was significant change in the yield but with further increase in time from 60 to 75 min there was not much noticeable impact of the process variable A but rather on the process variable D, i.e., there was significant impact on the biodiesel yield when the catalyst loading was increased from 6 to 8 wt.%, can be interpreted from Figure 11. Therefore, based on overall steepness in the slope and ANOVA

study, A has a dominant effect among all the variables causing a discernible impact on biodiesel yield.

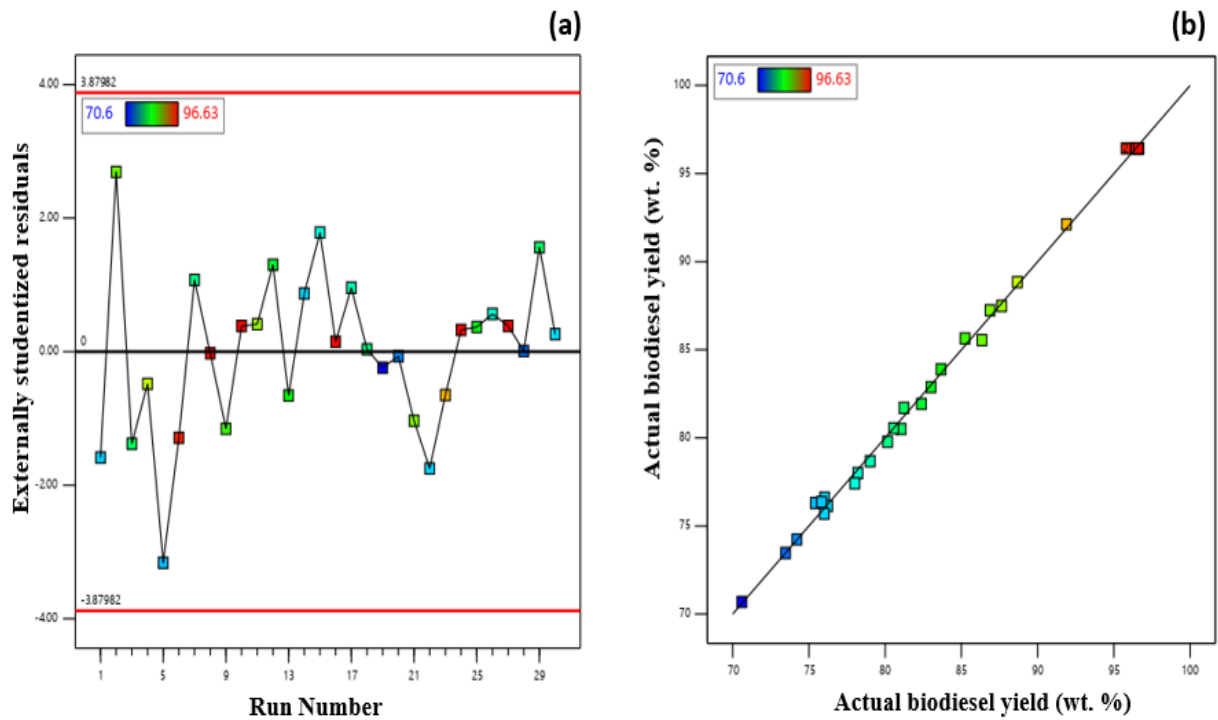


Figure 10. (a) Studentized residuals Vs. Run number and (b) Actual Vs. Predicted biodiesel yield (wt.%).

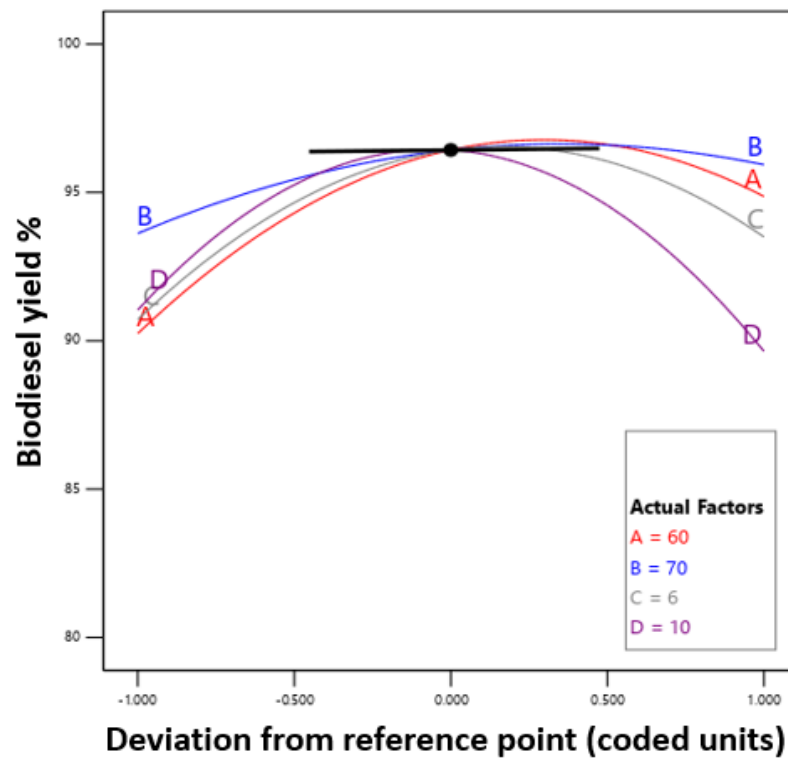


Figure 11. Perturbation plot exhibiting significant variables affecting biodiesel yield%.

2.4.1. Interaction of Input Variables

The effect of the four independent variables (time, temperature, catalyst loading (CL) and MTOR) on the biodiesel yield was examined by surface–model plots. Figure 12 shows the effect of time, temperature, catalyst loading, and MTOR on the biodiesel yield. The interaction of two variables in the model graphs can be observed, keeping other parameters constant at their centre values. Time is an important parameter, and it was observed from the surface graphs that as time increased, varying from 45–75 min, the biodiesel yield also increased up to the optimum point of 60 min, beyond which there was decrease in the yield despite the increase in the corresponding parameter values of temperature, catalyst loading and MTOR. The effect of temperature on the yield of biodiesel was investigated by varying temperature over the range 60 °C to 80 °C. The combined effect of temperature in Figure 12a, d showed a linear relationship with time and catalyst loading while in Figure 12e an increase in MTOR and temperature beyond the centre points cause a significant decrease in the yield. This could possibly be anticipated as due to reduction in the frequency of collisions of catalyst active sites and reactants due to increased amount of methanol in the reaction [47]. The combined effect of catalyst loading was observed by varying the catalyst amount from 4–8 wt.%, where the optimum central point giving maximum yield was 6 wt.%. Corresponding parameters with respect to catalyst loading in Figure 12b, d, f displayed an increase in biodiesel yield until the maximum was reached, following a linear relationship with other parameters. The decrease in yield due to the increase in catalyst loading could be due to an increase in the viscosity of the reaction mixture restricting mass transfer [48]. The interactive effect of MTOR with other parameters (Figure 12c,e,f) also displayed a linear correlation and biodiesel yield was observed to decrease after the central points of the maximum (MTOR– 10:1, CL 10 wt.%, time 60 min and temperature 70 °C) were reached.

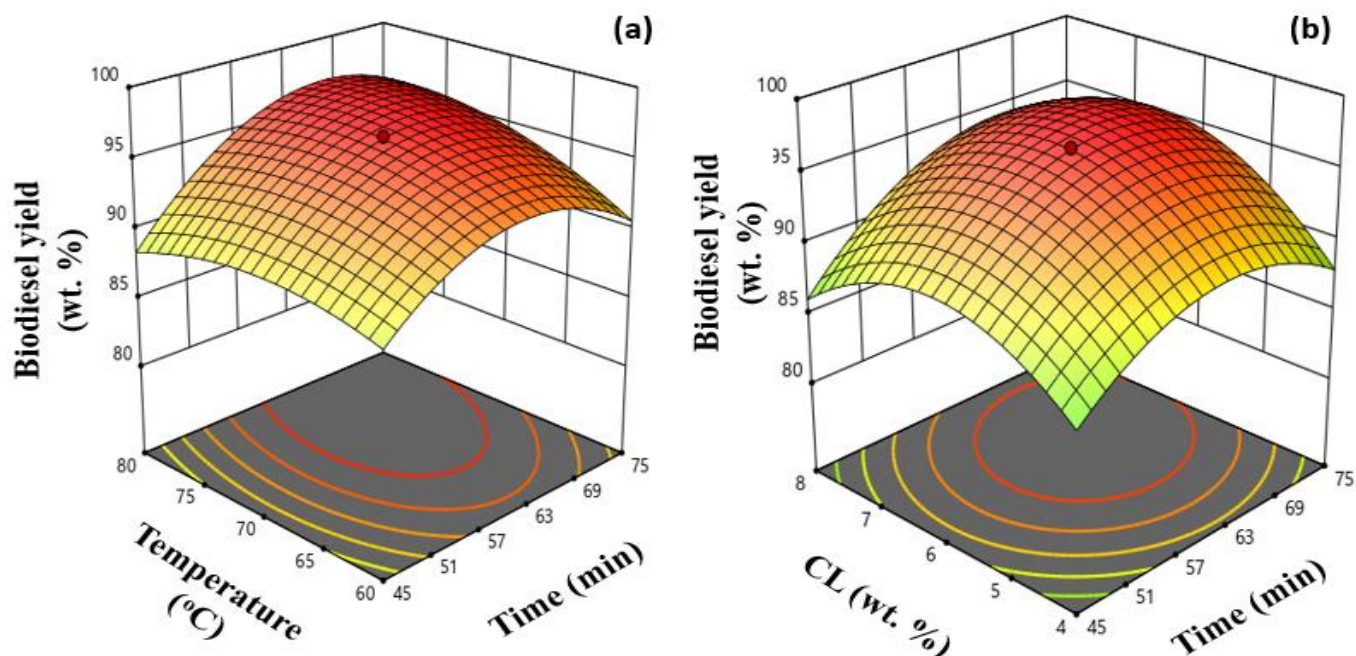


Figure 12. Cont.

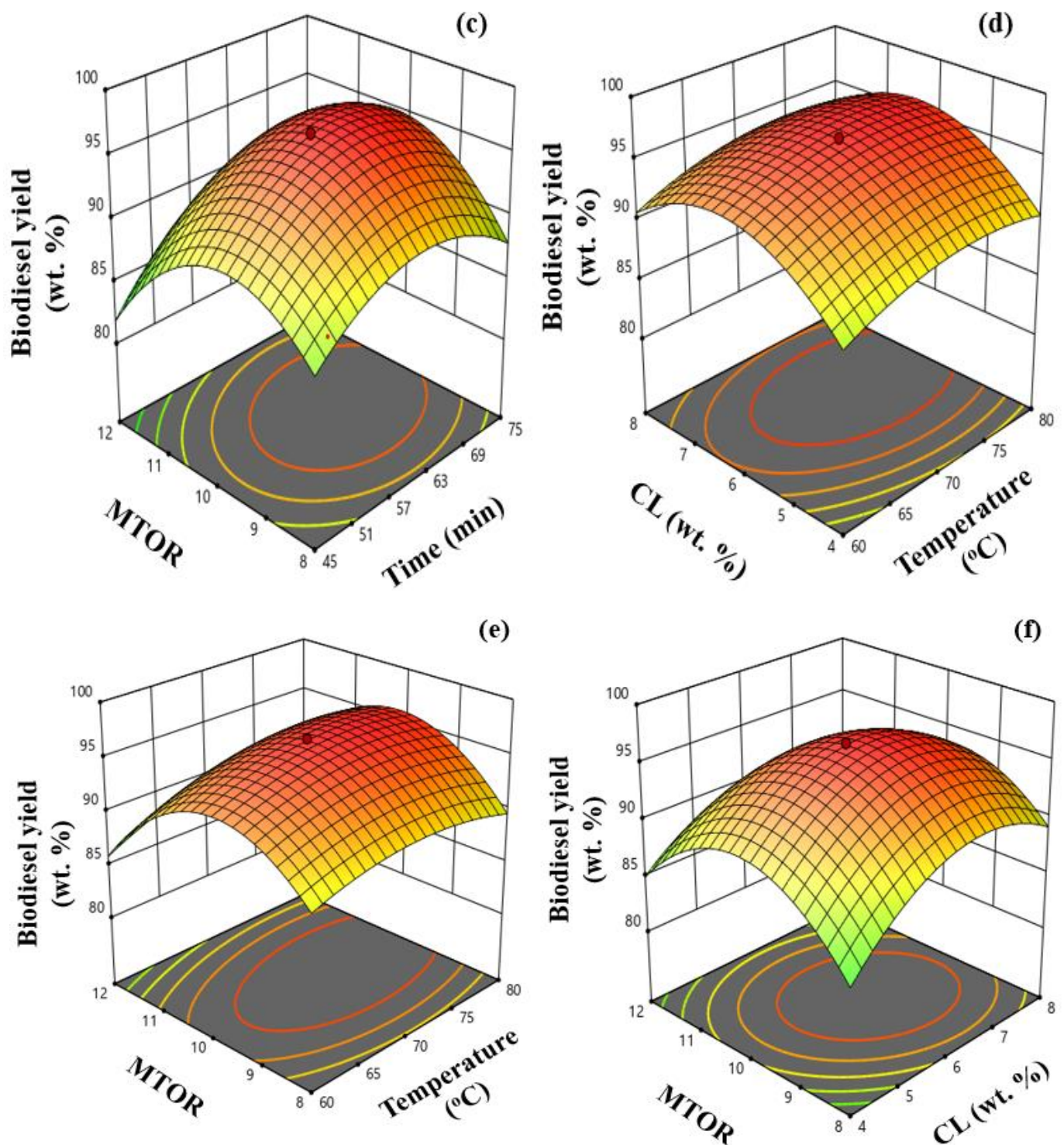


Figure 12. Surface plots of biodiesel yield with respect to MTOR, CL, time, and temperature (a–f).

2.4.2. Optimization of Biodiesel Yield

In this study, numerical optimization approach was followed to find the optimum conditions of the four input variables carrying a desirability function of 1. The goal of the optimization strategy was to optimize biodiesel yield while operating within the lower and upper bounds of the study's variable ranges. As RSM is a local optimizing method, it finds the optimum condition within the chosen range of variables. The optimal condition provided by the RSM–CCD approach for the transesterification of soybean oil was a

reaction time of 66.2 min, a reaction temperature of 73.2 °C, CL of 6.5 wt.% and an MTOR of 9.7 under microwave irradiation, with a biodiesel yield of 99.43 wt.%. This condition was used to conduct laboratory trials in triplicate, with an average biodiesel yield of 97.22 ± 0.4 wt.%, indicating that the regression model generated is effective in explaining the transesterification process.

2.5. Kinetics of Soybean–Oil Transesterification

The linear relationships between $-\ln(1-X)$ and time for reactions carried out at 60–100 °C are shown in Figure 13a, confirming our prediction that esterification proceeded through pseudo–first–order kinetics [49]. The activation energy (E_a) of the transesterification reaction was calculated by fitting rate constants to the Arrhenius equation (Equation (6)). The slope ($-E_a/R$) and intercept of the $\ln k$ vs. T^{-1} plot confirmed pseudo–first–order kinetics and yielded the activation energy E_a and the pre–exponential factor for the reaction. From Figure 13b, E_a was 31.54 kJmol^{-1} , and the pre–exponential factor was calculated to be $6.3 \times 10^3 \text{ min}^{-1}$.

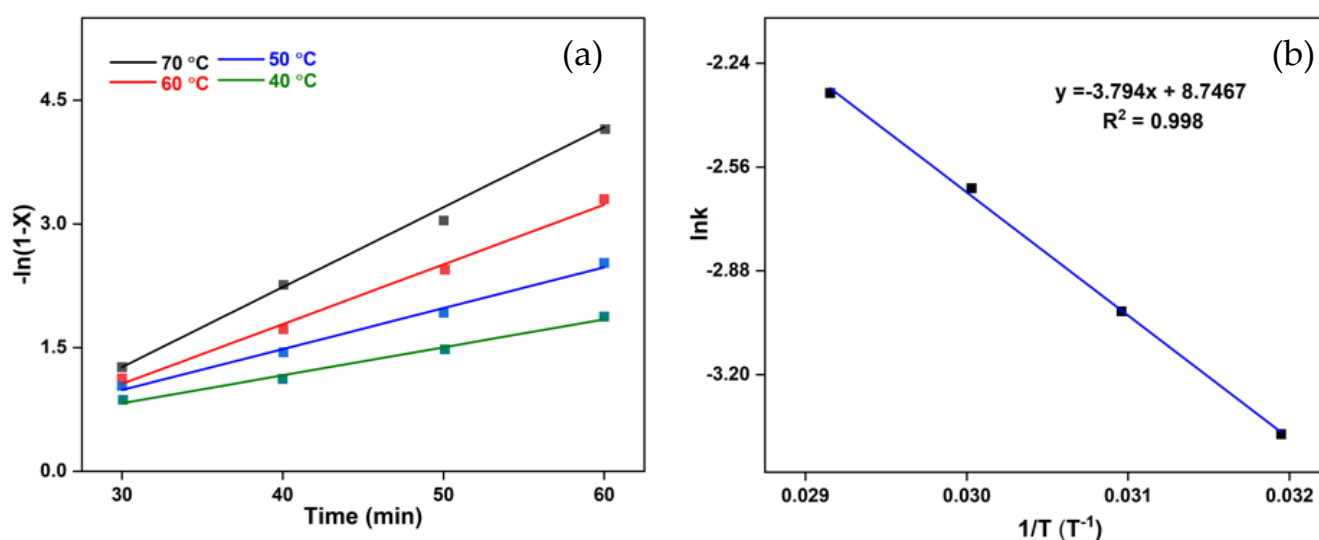


Figure 13. (a) $-\ln(1-X)$ vs. time (X = soybean yield) and the relevant Arrhenius plot of (b) $\ln k$ vs. $1/T$.

2.6. Comparison of Other Reported Heterogeneous Catalysts with the Present Catalyst

A variety of heterogeneous catalysts have been used to produce biodiesel, according to the literature. Table 5 summarizes the relevant details (i.e., type of catalyst, feedstock, operating parameters, turnover frequency (TOF), and biodiesel production) for comparison with other catalyst designed here. As compared to the catalyst, several other catalysts mentioned in the literature, such as peanut shell [14], AIL/HPMo/MIL–100(Fe) [50], MgO@ZnO [51], KNa/ZIF–8@GO [52] and $\text{K}_2\text{O}/\text{CaO}-\text{ZnO}$ [53], required a longer reaction time and higher temperature to produce biodiesel. The analysis of catalyst activity, TOF (turnover frequency; see SI Equation (S1), for our reported catalyst was $0.019 \text{ mol g}^{-1} \text{ h}^{-1}$, which was greater than many of the specified catalysts and probably better than a variety of catalysts provided in Table 5. Despite having a higher TOF than the current catalyst, AIL@NH₂–UiO–66 [54] and S–ZrO₂/SBA–15 [55] produced less biodiesel yield and also required a longer reaction time or higher temperature, respectively.

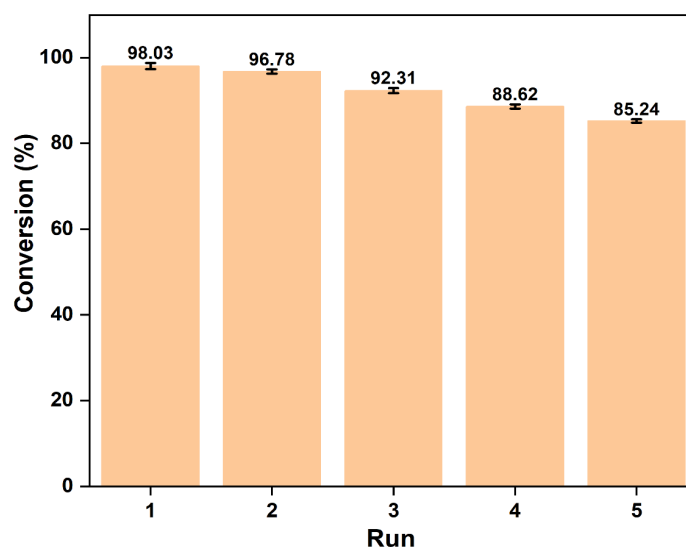
Table 5. Comparison of different heterogeneous catalysts for biodiesel production.

Entry	Catalyst	Feedstock	^a Conditions	TOF (mol g ⁻¹ h ⁻¹)	Biodiesel Yield (%)	Ref.
1.	Peanut shell	Algal oil	20:1, 5, 65, 4	0.005	94.91	[14]
2.	AIL–HPMo–MIL–100(Fe)	Soybean oil	30:1, 9, 120, 8	0.002	92.30	[50]
3.	AIL@NH ₂ –UiO–66	Oleic acid	14:1, 5, 75, 2	0.034	97.52	[54]
4.	MgO@ZnO	Soybean oil	3:1, 1, 210, 2	0.042	73.30	[51]
5.	CaO–MIL–100(Fe)	Palm oil	9:1, 4, 65, 2	0.014	95.09	[39]
6.	KNa/ZIF–8@GO	Soybean oil	18:1, 8, 100, 8	0.002	98.00	[52]
7.	Zn–CaO	Eucalyptus oil	6:1, 5, 65, 2.5	0.048	93.80	[56]
8.	K ₂ O/CaO–ZnO	Soybean oil	15:1, 6, 60, 4	0.004	81.10	[53]
9.	Cu–Ni–ZrO ₂	<i>Capparis spinosa</i> seed oil	6:1, 2.5, 70, 1.5	–	90.20	[57]
10.	ZrO ₂ /BLA	Soybean oil	15:1, 12, 50, 0.5	0.018	96.90	[58]
11.	CCPA	Hanne seed oil	15:1, 4.5, 65, 1.5	–	98.98	[59]
12.	SO ₄ /Fe–Al–TiO ₂	WCO	10:1, 3, 90, 2.5	0.013	96.00	[60]
13.	S–ZrO ₂ /SBA–15	WCO	10:1, 2, 140, 0.17	0.287	96.38	[55]
14.	CaO–ZrO ₂	Soybean oil	9.7:1, 6.5, 73.2, 1.1	0.019	97.22	This work

^a MTOR, Catalyst loading (wt.%), Temperature (°C), Time (h). AIL– Acidic ionic liquid. BLA– Bamboo leaf ash. CCPA– Cocoa pod husk–plantain peel ash. WCO– waste cooking oil.

2.7. Catalytic Reusability

Heterogeneous catalysts are reusable in nature, thus lowering the overall cost of the chemical reaction. For investigating the recyclability of CaO–ZrO₂, the catalyst used was isolated and recovered from the reaction mixture after each reaction cycle by filtration followed by washing with hexanol and drying in an oven for 5 h at 80 °C. Further, the catalyst was activated by calcining it at 500 °C. The catalyst was then used for the next four successive catalytic cycles by performing the same chemical reaction under the optimized reaction conditions and with the same recovery method (Figure 14). The SEM–EDS analysis of the reused catalyst (Figure S5) after five transesterification cycles indicated a decrease in the amount of calcium and zirconium ions. The deactivation of the catalyst mainly arises due to active–site blockage during the course of a reusability cycle and the leaching of metal ions. With the present reported catalyst CaO–ZrO₂, the leaching of Ca and Zr was investigated using ICP–AES analysis and found to be 4.7 ppm and <0.01 ppm in the biodiesel, respectively. This lesser amount of leaching of Ca in synthesized biodiesel critically meant that the UiO–66 MOF was used as sacrificial template to form ZrO₂, having carbon support prevented the leaching of CaO to a significant extent.

**Figure 14.** Reusability of CaO–ZrO₂ catalyst in the transesterification of soybean oil over 5 cycles.

3. Materials and Methods

3.1. Chemicals Used

Soybean oil was purchased from a local market in Silchar, Assam, India. Waste snail shells (*Pila* spp.) were procured from Mizoram, India. Zirconium oxychloride octahydrate and terephthalic acid were purchased from Sigma Aldrich, Bengaluru, India. Dimethyl formamide, acetic acid and methanol (analytical grade) were purchased from Merck, Silchar, India. The chemicals were used without further purification.

3.2. Preparation of UiO-66 MOF

The UiO-66 MOF was prepared according to the literature [61]. Zirconium (IV) oxychloride octahydrate (1.61 g, 5.0 mmol) and benzene-1, 4-dicarboxylic acid (1.20 g, 7.25 mmol) were dissolved in N, N-dimethylformamide (30 mL, 99%) and stirred for 30 min. Concentrated hydrochloric acid (1.5 mL, 37%) and glacial acetic acid (2.0 mL) were added with vigorous stirring and the resulting solution was sealed in a 100 mL Pyrex Schott bottle, which was kept in an oven for 2 h at 100 °C. This yielded UiO-66 as a thick white gel. N, N-dimethylformamide (50 mL) was added to the UiO-66 gel and vigorously mixed. The diluted UiO-66 suspension (7 mL per tube) was centrifuged for 10 min at 4000 rpm, and the supernatant was decanted. The gel was washed further with methanol (10 min, 4000 rpm) and dried in a vacuum oven for 6 h at 100 °C to produce UiO-66.

3.3. Preparation of Snail-Shell-Derived CaO

The preparatory method followed was in accordance with our previous paper [13] where the obtained snail shells were cleaned with distilled water multiple times to remove undesirable contaminants and dried in an oven for 12 h at 100 °C. The snail shells were then crushed into a fine powder using a mortar and pestle, sieved (with a mesh size of 125–250 µm), and then calcined for 4 h at 900 °C in a muffle furnace to obtain CaO.

3.4. Preparation of MOF-Based CaO-ZrO₂ Composite Catalyst

The catalyst was synthesized by the wet impregnation method by dispersing 0.5 g of UiO-66 in 30 ml of distilled water and certain amount of snail-shell-derived CaO (30, 40, 50, 60, 70 wt.%) was added into the solution and stirred vigorously at 30 °C for 10 h. The resultant mixture was then placed into an air-dry oven at 100 °C for 16 h with catalyst precursor formation. Afterwards, the precursor was put into a tubular furnace in an inert N₂ atmosphere, where it was kept at different temperature ranges of 600 °C, 650 °C, 700 °C and 750 °C to obtain an optimum activation temperature.

3.5. Catalyst Characterization

An XPert Pro diffractometer was employed for X-ray powder diffraction (XRD) using Cu K α radiation with $2\theta = 7-70^\circ$. The operating current and voltage were 100 mA and 40 kV, respectively. A QuantaChrome Nova 2200e Surface Area and Pore Size Analyzer was employed to determine surface area and total pore volume using Brunauer-Emmet-Teller (BET) analysis. Mettler Toledo TGA / DSC was employed for TGA and performed in the range 20–700 °C with a heating rate of 5 °C min⁻¹ under a continuous flow of nitrogen. Functional groups were identified in the samples using Fourier transform infrared (FTIR) analysis and IR spectra were recorded in the range 400–4000 cm⁻¹ with a 3000 Hyperion FTIR spectrometer (Bruker, Germany). The morphology of the catalyst was evaluated with scanning electron microscopy (SEM) equipped with energy-dispersive X-ray spectroscopy (EDS) and elemental mapping using an FEI-Quanta FEG 200F microscope operating at 100 mA beam current, 30 kV and 5000 \times magnification. Transmission electron microscopy (TEM) images were captured on a JEOL JEM-2100 microscope. X-ray photoelectron spectroscopy (XPS) was evaluated using a K-alpha XPS spectrometer (Thermo) with a monochromatic Al K α X-ray source.

3.6. Biodiesel Production from Transesterification of Soybean Oil

In a 10 mL microwave tube, soybean oil (0.874 g, 1 mmol), methanol (0.32 g, 10 mmol) and catalyst (52.4 mg, 6 wt.% with respect to soybean oil) were added. The reaction mixture was held in a microwave reactor (Discover SP Microwave System, Delhi, India) for 60 min at 70 °C, 100 psi pressure and 50 W power, following which the catalyst was separated by filtration. The product was then concentrated using a rotary evaporator to remove excess methanol.

3.7. Biodiesel Characterization

¹H and ¹³C NMR spectroscopy was used to identify the transesterification product, biodiesel. A Bruker Avance spectrometer (500 MHz) was employed for the analyses. A gas chromatogram (GC) was used to identify types of methyl esters converted from triglyceride. The temperature of the oven was kept in the range 60–280 °C and the injector and detector temperature were maintained at 200 °C and 300 °C, respectively. Fourier transform infrared (FT–IR) was used to identify the characteristic peaks of biodiesel generated from soybean oil.

3.8. Reaction Kinetics

Due to the abundance of methanol, pseudo–first–order kinetics followed the transesterification process, allowing the backward process to be neglected. Thus, the rate of the reaction ($-r_{OA}$) could be expressed as:

$$-r_{OA} = -\frac{d[OA]}{dt} = k[SO] \quad (4)$$

The rate constant is k , the concentration of soybean oil is $[SO]$, and the reaction time is t . Monitoring methyl ester (ME) yield and thus the yield of soybean oil at varied time t in (Equation (5)) yielded the first–order rate constant (k). The Arrhenius equation (Equation (6)) along with k at various temperatures (60–100 °C) were applied to calculate activation energy (E_a).

$$-\ln(1 - X) = kt \quad (5)$$

$$\ln k = -\frac{E_a}{RT} + \ln A \quad (6)$$

Here, soybean–oil yield at time t is represented by X , the pre–exponential factor by A , the reaction temperature by T and R is $8.314 \times 10^{-3} \text{ kJ K}^{-1} \text{ mol}^{-1}$.

3.9. Modelling of the Transesterification Process

The effect of process variables such as the methanol–to–oil ratio (MTOR), catalyst loading, temperature and reaction time on the biodiesel yield was investigated using central composite design (CCD). The independent variables selected were MTOR with a range of 8:1–12:1, catalyst loading with a range of 4–8 wt.%, temperature with a range of 60–80 °C and reaction time with a range of 45–75 min, and biodiesel yield was inserted as the response. Factorial design with five levels and four factors was used, providing 30 randomized experimental conditions to reduce variability effect in the observed response. The design includes six centre points to test the repeatability of the method. The distance of the axial point (α) from each design variable was ± 0.05 . To define the quadratic model of the response, the experimental data were analysed using the multiple regression method. The attributes of the fitted model were evaluated using analysis of variance (ANOVA). Design Expert version 13.0 (Stat–Ease Inc., Minneapolis, MN, USA) software was used for the regression analysis of the model.

4. Fuel Properties of Biodiesel

The fuel properties of biodiesel, such as density, flash point, kinematic viscosity (at 40 °C), calorific value and acid value, were measured as per ASTM–D6751 standards. The

measured physicochemical biodiesel properties are given in Table 6. All the property values lie within the limits of the ASTM biodiesel standard and thus possess the potential to be used in transport engines as an alternative fuel.

Table 6. Comparison of physicochemical properties of produced biodiesel with ASTM D6571 standards.

Properties	ASTM Standards	Biodiesel (This Study)
Density (kg/m ³)	860–900	865
Flash point (°C)	>130	161
Kinematic viscosity at 40 °C (mm ² /s)	1.9–6	4.08
Calorific value (MJ/kg)	35–45	42.24
Acid value (mg KOH/g)	Max. 0.5	0.42

5. Conclusions

In this present work, using MOF and biomass-derived ZrO₂-supported CaO, a heterogeneous nanocatalyst, CaO–ZrO₂, was successfully synthesized for the conversion of soybean oil to biodiesel by transesterification process. The prepared catalyst showed an excellent activity for the transesterification of biodiesel with 98.03 ± 0.7% conversion and a yield of 97.22 ± 0.4% under optimized reaction conditions as predicted by RSM numerical optimization process under microwave irradiation. The high basicity of 3.9 mmol g^{−1} of the catalyst triggered the transesterification of the soybean oil and resulted in the successful conversion into biodiesel with 9,12–octadecadienoic acid (Z, Z) methyl ester as one of the major constituents. The RSM–CCD–approach–based optimization process was an efficient way to enhance the biodiesel yield and revealed the reaction time and catalyst loading as two major sensitive factors to influence biodiesel yield for this kind of basic catalyst.

Supplementary Materials: The following supporting information can be downloaded at: <https://www.mdpi.com/article/10.3390/catal12111312/s1>, Figure S1: XPS survey spectrum of CaO-ZrO₂; Figure S2: XRD of (a) pure CaO and snail-shell-derived-CaO, (b) m-ZrO₂, t-ZrO₂, UiO-66 derived ZrO₂, and CaO-ZrO₂ catalyst; Figure S3: ¹H and ¹³C NMR spectra of the synthesized biodiesel; Figure S4: FT-IR spectrum of synthesized biodiesel; Figure S5: EDS spectrum of the recovered catalyst after 5 transesterification cycles.

Author Contributions: Writing-original draft, S.P.G., S.L.R. and A.D.; investigation: S.P.G. and S.L.R.; data analysis: S.P.G., J.M.H.A., P.K. and U.R.; conceptualization: S.P.G. and S.L.R.; reviewing: S.L.R., A.D., J.M.H.A. and U.R.; supervision: S.L.R. All authors have read and agreed to the published version of the manuscript.

Funding: This research received no specific grant from any funding agency.

Data Availability Statement: The datasets used to support the findings are included within the article and in the supplementary file.

Acknowledgments: Thanks University Grants Commission, New Delhi, India for the award of UGC-Assistant Professorship under Faculty Recharge Programme.

Conflicts of Interest: The authors confirm no conflict of interest.

References

- Changmai, B.; Wheatley, A.E.H.; Rano, R.; Halder, G.; Selvaraj, M.; Rashid, U.; Rokhum, S.L. A Magnetically Separable Acid-Functionalized Nanocatalyst for Biodiesel Production. *Fuel* **2021**, *305*, 121576. [CrossRef]
- Jamil, U.; Husain Khoja, A.; Liaquat, R.; Raza Naqvi, S.; Nor Nadyaini Wan Omar, W.; Aishah Saidina Amin, N. Copper and Calcium-Based Metal Organic Framework (MOF) Catalyst for Biodiesel Production from Waste Cooking Oil: A Process Optimization Study. *Energy Convers. Manag.* **2020**, *215*, 112934. [CrossRef]
- Changmai, B.; Rano, R.; Vanlalveni, C.; Rokhum, L. A Novel Citrus Sinensis Peel Ash Coated Magnetic Nanoparticles as an Easily Recoverable Solid Catalyst for Biodiesel Production. *Fuel* **2021**, *286*, 119447. [CrossRef]

4. Ma, X.; Liu, F.; Helian, Y.; Li, C.; Wu, Z.; Li, H.; Chu, H.; Wang, Y.; Wang, Y.; Lu, W.; et al. Current Application of MOFs Based Heterogeneous Catalysts in Catalyzing Transesterification/Esterification for Biodiesel Production: A Review. *Energy Convers. Manag.* **2021**, *229*. [[CrossRef](#)]
5. Liu, F.; Ma, X.; Li, H.; Wang, Y.; Cui, P.; Guo, M.; Yaxin, H.; Lu, W.; Zhou, S.; Yu, M. Dilute Sulfonic Acid Post Functionalized Metal Organic Framework as a Heterogeneous Acid Catalyst for Esterification to Produce Biodiesel. *Fuel* **2020**, *266*. [[CrossRef](#)]
6. Li, H.; Liu, F.; Ma, X.; Cui, P.; Guo, M.; Li, Y.; Gao, Y.; Zhou, S.; Yu, M. An Efficient Basic Heterogeneous Catalyst Synthesis of Magnetic Mesoporous Fe@C Support SrO for Transesterification. *Renew. Energy* **2020**, *149*, 816–827. [[CrossRef](#)]
7. Zhang, Q.; Zhang, Q.; Yang, T.; Lei, D.; Wang, J.; Zhang, Y.; Zhang, Y. Efficient Production of Biodiesel from Esterification of Lauric Acid Catalyzed by Ammonium and Silver Co-Doped Phosphotungstic Acid Embedded in a Zirconium Metal-Organic Framework Nanocomposite. *ACS Omega* **2020**, *5*, 12760–12767. [[CrossRef](#)]
8. Wan, H.; Chen, C.; Wu, Z.; Que, Y.; Feng, Y.; Wang, W.; Wang, L.; Guan, G.; Liu, X. Encapsulation of Heteropolyanion-Based Ionic Liquid within the Metal-Organic Framework MIL-100(Fe) for Biodiesel Production. *ChemCatChem* **2015**, *7*, 441–449. [[CrossRef](#)]
9. Stamenković, O.S.; Veličković, A.V.; Veljković, V.B. The Production of Biodiesel from Vegetable Oils by Ethanolysis: Current State and Perspectives. *Fuel* **2011**. [[CrossRef](#)]
10. Gouda, S.P.; Ngaosuwan, K.; Assabumrungrat, S.; Selvaraj, M.; Halder, G.; Rokhum, S.L. Microwave Assisted Biodiesel Production Using Sulfonic Acid-Functionalized Metal-Organic Frameworks UiO-66 as a Heterogeneous Catalyst. *Renew. Energy* **2022**, *197*, 161–169. [[CrossRef](#)]
11. Lee, S.L.; Wong, Y.C.; Tan, Y.P.; Yew, S.Y. Transesterification of Palm Oil to Biodiesel by Using Waste Obtuse Horn Shell-Derived CaO Catalyst. *Energy Convers. Manag.* **2015**, *93*, 282–288. [[CrossRef](#)]
12. Rafiei, S.; Tangestaninejad, S.; Horcajada, P.; Moghadam, M.; Mirkhani, V.; Mohammadpoor-Baltork, I.; Kardanpour, R.; Zadehahmadi, F. Efficient Biodiesel Production Using a Lipase@ZIF-67 Nanobioreactor. *Chem. Eng. J.* **2018**, *334*. [[CrossRef](#)]
13. Laskar, I.B.; Rajkumari, K.; Gupta, R.; Chatterjee, S.; Paul, B.; Rokhum, L. Waste Snail Shell Derived Heterogeneous Catalyst for Biodiesel Production by the Transesterification of Soybean Oil. *RSC Adv.* **2018**, *8*, 20131–20142. [[CrossRef](#)] [[PubMed](#)]
14. Behera, B.; Dey, B.; Balasubramanian, P. Algal Biodiesel Production with Engineered Biochar as a Heterogeneous Solid Acid Catalyst. *Bioresour. Technol.* **2020**, *310*, 123392. [[CrossRef](#)] [[PubMed](#)]
15. Zhang, Q.; Lei, D.; Luo, Q.; Wang, J.; Deng, T.; Zhang, Y.; Ma, P. Efficient biodiesel production from oleic acid using metal-organic framework encapsulated Zr-doped polyoxometalate nano-hybrids. *RSC Adv.* **2020**, *10*, 8766–8772. [[CrossRef](#)]
16. Nanda, M.R.; Zhang, Y.; Yuan, Z.; Qin, W.; Ghaziaskar, H.S.; Xu, C. Catalytic Conversion of Glycerol for Sustainable Production of Solketal as a Fuel Additive: A Review. *Renew. Sustain. Energy Rev.* **2016**, *56*, 1022–1031. [[CrossRef](#)]
17. Ooi, X.Y.; Gao, W.; Ong, H.C.; Lee, H.V.; Juan, J.C.; Chen, W.H.; Lee, K.T. Overview on Catalytic Deoxygenation for Biofuel Synthesis Using Metal Oxide Supported Catalysts. *Renew. Sustain. Energy Rev.* **2019**, *112*, 834–852. [[CrossRef](#)]
18. Sahani, S.; Roy, T.; Sharma, Y.C. Smart Waste Management of Waste Cooking Oil for Large Scale High Quality Biodiesel Production Using Sr-Ti Mixed Metal Oxide as Solid Catalyst: Optimization and E-Metrics Studies. *Waste Manag.* **2020**, *108*, 189–201. [[CrossRef](#)]
19. Niju, S.; Raj, F.R.; Anushya, C.; Balajii, M. Optimization of Acid Catalyzed Esterification and Mixed Metal Oxide Catalyzed Transesterification for Biodiesel Production from Moringa Oleifera Oil. *Green Process. Synth.* **2019**, *8*, 756–775. [[CrossRef](#)]
20. Sedaghat-Hoor, S.; Anbia, M. ZnO Impregnated MgAl(O) Catalyst with Improved Properties for Biodiesel Production: The Influence of Synthesis Method on Stability and Reusability. *Part. Sci. Technol.* **2018**, *37*, 893–899. [[CrossRef](#)]
21. Gutiérrez-Ortega, N.; Ramos-Ramírez, E.; Serafin-Muñoz, A.; Zamorategui-Molina, A.; Monjaraz-Vallejo, J. Use of Co/Fe-Mixed Oxides as Heterogeneous Catalysts in Obtaining Biodiesel. *Catalysts* **2019**, *9*, 403. [[CrossRef](#)]
22. Ooi, H.K.; Koh, X.N.; Ong, H.C.; Lee, H.V.; Mastuli, M.S.; Taufiq-Yap, Y.H.; Alharthi, F.A.; Alghamdi, A.A.; Mijan, N.A. Progress on Modified Calcium Oxide Derived Waste-Shell Catalysts for Biodiesel Production. *Catalysts* **2021**, *11*, 194. [[CrossRef](#)]
23. Noiroj, K.; Intarapong, P.; Luengnaruemitchai, A.; Jai-In, S. A Comparative Study of KOH/Al₂O₃ and KOH/NaY Catalysts for Biodiesel Production via Transesterification from Palm Oil. *Renew. Energy* **2009**, *34*, 1145–1150. [[CrossRef](#)]
24. Liu, L.; Wen, Z.; Cui, G. Preparation of Ca/Zr Mixed Oxide Catalysts through a Birch-Templating Route for the Synthesis of Biodiesel via Transesterification. *Fuel* **2015**, *158*, 176–182. [[CrossRef](#)]
25. Wang, H.; Wang, M.; Liu, S.; Zhao, N.; Wei, W.; Sun, Y. Influence of Preparation Methods on the Structure and Performance of CaO–ZrO₂ Catalyst for the Synthesis of Dimethyl Carbonate via Transesterification. *J. Mol. Catal. A Chem.* **2006**, *258*, 308–312. [[CrossRef](#)]
26. Rahman, N.J.A.; Ramli, A.; Jumbri, K.; Uemura, Y. Tailoring the Surface Area and the Acid–Base Properties of ZrO₂ for Biodiesel Production from Nannochloropsis Sp. *Sci. Rep.* **2019**, *9*, 1–12. [[CrossRef](#)]
27. Bellido, J.D.A.; De Souza, J.E.; M'Peko, J.C.; Assaf, E.M. Effect of Adding CaO to ZrO₂ Support on Nickel Catalyst Activity in Dry Reforming of Methane. *Appl. Catal. A Gen.* **2009**, *358*, 215–223. [[CrossRef](#)]
28. Xia, S.; Guo, X.; Mao, D.; Shi, Z.; Wu, G.; Lu, G. Biodiesel Synthesis over the CaO–ZrO₂ Solid Base Catalyst Prepared by a Urea–Nitrate Combustion Method. *RSC Adv.* **2014**, *4*, 51688–51695. [[CrossRef](#)]
29. Huang, Y.B.; Liang, J.; Wang, X.S.; Cao, R. Multifunctional Metal–Organic Framework Catalysts: Synergistic Catalysis and Tandem Reactions. *Chem. Soc. Rev.* **2017**, *46*, 126–157. [[CrossRef](#)]
30. Stock, N.; Biswas, S. Synthesis of Metal–Organic Frameworks (MOFs): Routes to Various MOF Topologies, Morphologies, and Composites. *Chem. Rev.* **2012**, *112*, 933–969. [[CrossRef](#)]

31. Dhakshinamoorthy, A.; Santiago-Portillo, A.; Asiri, A.M.; Garcia, H. Engineering UiO-66 Metal Organic Framework for Heterogeneous Catalysis. *ChemCatChem* **2019**, *11*, 899–923. [[CrossRef](#)]
32. Chen, D.; Sun, H.; Wang, Y.; Quan, H.; Ruan, Z.; Ren, Z.; Luo, X. UiO-66 Derived Zirconia/Porous Carbon Nanocomposites for Efficient Removal of Carbamazepine and Adsorption Mechanism. *Appl. Surf. Sci.* **2020**, *507*, 145054. [[CrossRef](#)]
33. Liu, S.; Ma, J.; Guan, L.; Li, J.; Wei, W.; Sun, Y. Mesoporous CaO-ZrO₂ Nano-Oxides: A Novel Solid Base with High Activity and Stability. *Microporous Mesoporous Mater.* **2009**, *117*, 466–471. [[CrossRef](#)]
34. Jannah, I.N.A.; Sekarsari, H.F.; Mulijani, S.; Wijaya, K.; Wibowo, A.C.; Patah, A. Facile Synthesis of Various ZrO₂ Phases and ZrO₂-MO₂ (M = Ti, Hf) by Thermal Decomposition of a Single UiO-66 Precursor for Photodegradation of Methyl Orange. *Catalysts* **2022**, *12*, 609. [[CrossRef](#)]
35. Li, H.; Wang, Y.; Ma, X.; Guo, M.; Li, Y.; Li, G.; Cui, P.; Zhou, S.; Yu, M. Synthesis of CaO/ZrO₂ Based Catalyst by Using UiO-66(Zr) and Calcium Acetate for Biodiesel Production. *Renew. Energy* **2022**, *185*, 970–977. [[CrossRef](#)]
36. Zhang, Q.; Zhang, Y.; Li, H.; Gao, C.; Zhao, Y. Heterogeneous CaO-ZrO₂ Acid-Base Bifunctional Catalysts for Vapor-Phase Selective Dehydration of 1,4-Butanediol to 3-Buten-1-ol. *Appl. Catal. A Gen.* **2013**, *466*, 233–239. [[CrossRef](#)]
37. Wang, J.; Li, G.; Li, Z.; Tang, C.; Feng, Z.; An, H.; Liu, H.; Liu, T.; Li, C. A Highly Selective and Stable ZnO-ZrO₂ Solid Solution Catalyst for CO₂ Hydrogenation to Methanol. *Sci. Adv.* **2017**, *3*. [[CrossRef](#)]
38. Wang, H.; Wang, M.; Zhao, N.; Wei, W.; Sun, Y. CaO-ZrO₂ Solid Solution: A Highly Stable Catalyst for the Synthesis of Dimethyl Carbonate from Propylene Carbonate and Methanol. *Catal. Lett.* **2005**, *105*, 253–257. [[CrossRef](#)]
39. Li, H.; Wang, Y.; Ma, X.; Wu, Z.; Cui, P.; Lu, W.; Liu, F.; Chu, H.; Wang, Y. A Novel Magnetic CaO-Based Catalyst Synthesis and Characterization: Enhancing the Catalytic Activity and Stability of CaO for Biodiesel Production. *Chem. Eng. J.* **2020**, *391*, 123549. [[CrossRef](#)]
40. Ge, J.; Liu, L.; Shen, Y. Facile Synthesis of Amine-Functionalized UiO-66 by Microwave Method and Application for Methylene Blue Adsorption. *J. Porous Mater.* **2017**, *24*, 647–655. [[CrossRef](#)]
41. Fang, X.; Wu, S.; Wu, Y.; Yang, W.; Li, Y.; He, J.; Hong, P.; Nie, M.; Xie, C.; Wu, Z.; et al. High-Efficiency Adsorption of Norfloxacin Using Octahedral UiO-66-NH₂ Nanomaterials: Dynamics, Thermodynamics, and Mechanisms. *Appl. Surf. Sci.* **2020**, *518*, 146226. [[CrossRef](#)]
42. Zhou, D.; Chen, X.; Wei, X.; Tang, L.; Liang, J.; Wang, S.; Wang, L. Insights into the Synergetic Mechanism of Basic Active Site and Oxygen Vacancy on Thermally Activated MOFs for the Colophony Esterification: Experiments and DFT Calculations. *Ind. Crops Prod.* **2021**, *166*, 113486. [[CrossRef](#)]
43. Laskar, I.B.; Deshmukhya, T.; Bhanja, P.; Paul, B.; Gupta, R.; Chatterjee, S. Transesterification of Soybean Oil at Room Temperature Using Biowaste as Catalyst; an Experimental Investigation on the Effect of Co-Solvent on Biodiesel Yield. *Renew. Energy* **2020**, *162*, 98–111. [[CrossRef](#)]
44. Kaewdaeng, S.; Sintuya, P.; Nirunsin, R. Biodiesel Production Using Calcium Oxide from River Snail Shell Ash as Catalyst. *Energy Procedia* **2017**, *138*, 937–942.
45. Dhawane, S.H.; Kumar, T.; Halder, G. Parametric Effects and Optimization on Synthesis of Iron (II) Doped Carbonaceous Catalyst for the Production of Biodiesel. *Energy Convers. Manag.* **2016**, *122*, 310–320. [[CrossRef](#)]
46. Betiku, E.; Etim, A.O.; Perea, O.; Ojumu, T.V. Two-Step Conversion of Neem (*Azadirachta Indica*) Seed Oil into Fatty Methyl Esters Using a Heterogeneous Biomass-Based Catalyst: An Example of Cocoa Pod Husk. *Energy and Fuels* **2017**, *31*, 6182–6193. [[CrossRef](#)]
47. Li, Q.; Chen, Y.; Bai, S.; Shao, X.; Jiang, L.; Li, Q. Immobilized Lipase in Bio-Based Metal-Organic Frameworks Constructed by Biomimetic Mineralization: A Sustainable Biocatalyst for Biodiesel Synthesis. *Colloids Surfaces B Biointerfaces* **2020**, *188*. [[CrossRef](#)]
48. Li, H.; Niu, S.; Lu, C.; Li, J. Calcium Oxide Functionalized with Strontium as Heterogeneous Transesterification Catalyst for Biodiesel Production. *Fuel* **2016**, *176*, 63–71. [[CrossRef](#)]
49. Sharma, A.; Kodgire, P.; Kachhwaha, S.S. Biodiesel Production from Waste Cotton-Seed Cooking Oil Using Microwave-Assisted Transesterification: Optimization and Kinetic Modeling. *Renew. Sustain. Energy Rev.* **2019**, *116*, 109394. [[CrossRef](#)]
50. Xie, W.; Wan, F. Biodiesel Production from Acidic Oils Using Polyoxometalate-Based Sulfonated Ionic Liquids Functionalized Metal-Organic Frameworks. *Catal. Letters* **2019**, *100*. [[CrossRef](#)]
51. Yang, C.M.; Huynh, M.V.; Liang, T.Y.; Le, T.K.; Kieu Xuan Huynh, T.; Lu, S.Y.; Tsai, D.H. Metal-Organic Framework-Derived Mg-Zn Hybrid Nanocatalyst for Biodiesel Production. *Adv. Powder Technol.* **2022**, *33*, 103365. [[CrossRef](#)]
52. Fazaeli, R.; Aliyan, H. Production of Biodiesel through Transesterification of Soybean Oil Using ZIF-8@GO Doped with Sodium and Potassium Catalyst. *Russ. J. Appl. Chem.* **2015**, *88*. [[CrossRef](#)]
53. Istadi, I.; Prasetyo, S.A.; Nugroho, T.S. Characterization of K₂O/CaO-ZnO Catalyst for Transesterification of Soybean Oil to Biodiesel. *Procedia Environ. Sci.* **2015**, *23*, 394–399. [[CrossRef](#)]
54. Lu, P.; Li, H.; Li, M.; Chen, J.; Ye, C.; Wang, H.; Qiu, T. Ionic Liquid Grafted NH₂-UiO-66 as Heterogeneous Solid Acid Catalyst for Biodiesel Production. *SSRN Electron. J.* **2022**. [[CrossRef](#)]
55. Hossain, M.N.; Ullah Siddik Bhuyan, M.S.; Md Ashraf Alam, A.H.; Seo, Y.C. Biodiesel from Hydrolyzed Waste Cooking Oil Using a S-ZrO₂/SBA-15 Super Acid Catalyst under Sub-Critical Conditions. *Energies* **2018**, *11*, 299. [[CrossRef](#)]
56. Rahman, W.U.; Fatima, A.; Anwer, A.H.; Athar, M.; Khan, M.Z.; Khan, N.A.; Halder, G. Biodiesel Synthesis from Eucalyptus Oil by Utilizing Waste Egg Shell Derived Calcium Based Metal Oxide Catalyst. *Process Saf. Environ. Prot.* **2019**, *122*, 313–319. [[CrossRef](#)]

57. Munir, M.; Ahmad, M.; Saeed, M.; Waseem, A.; Nizami, A.S.; Sultana, S.; Zafar, M.; Rehan, M.; Srinivasan, G.R.; Ali, A.M.; et al. Biodiesel Production from Novel Non-Edible Caper (*Capparis Spinosa* L.) Seeds Oil Employing Cu–Ni Doped ZrO₂ Catalyst. *Renew. Sustain. Energy Rev.* **2021**, *138*, 110558. [[CrossRef](#)]
58. Fatimah, I.; Rubiyanto, D.; Taushiyah, A.; Najah, F.B.; Azmi, U.; Sim, Y.L. Use of ZrO₂ Supported on Bamboo Leaf Ash as a Heterogeneous Catalyst in Microwave-Assisted Biodiesel Conversion. *Sustain. Chem. Pharm.* **2019**, *12*, 100129. [[CrossRef](#)]
59. Olatundun, E.A.; Borokini, O.O.; Betiku, E. Cocoa Pod Husk-Plantain Peel Blend as a Novel Green Heterogeneous Catalyst for Renewable and Sustainable Honne Oil Biodiesel Synthesis: A Case of Biowastes-to-Wealth. *Renew. Energy* **2020**, *166*, 163–175. [[CrossRef](#)]
60. Gardy, J.; Osatiashtiani, A.; Céspedes, O.; Hassanpour, A.; Lai, X.; Lee, A.F.; Wilson, K.; Rehan, M. A Magnetically Separable SO₄/Fe-Al-TiO₂ Solid Acid Catalyst for Biodiesel Production from Waste Cooking Oil. *Appl. Catal. B Environ.* **2018**. [[CrossRef](#)]
61. Connolly, B.M.; Aragones-Anglada, M.; Gandara-Loe, J.; Danaf, N.A.; Lamb, D.C.; Mehta, J.P.; Vulpe, D.; Wuttke, S.; Silvestre-Albero, J.; Moghadam, P.Z.; et al. Tuning Porosity in Macroscopic Monolithic Metal-Organic Frameworks for Exceptional Natural Gas Storage. *Nat. Commun.* **2019**, *10*. [[CrossRef](#)]